Delft University of Technology

Multiphase transient analysis for monitoring of CO_2 flooding

Li, Longlong; Voskov, Denis; Yao, Jun; Li, Yang

DOI
10.1016/j.petrol.2017.10.075

Publication date
2018

Document Version
Final published version

Published in
Journal of Petroleum Science and Engineering

Citation (APA)
Li, L., Voskov, D., Yao, J., & Li, Y. (2018). Multiphase transient analysis for monitoring of CO_2 flooding. *Journal of Petroleum Science and Engineering*, *160*, 537-554. https://doi.org/10.1016/j.petrol.2017.10.075

Important note
To cite this publication, please use the final published version (if applicable).
Please check the document version above.

Copyright
Other than for strictly personal use, it is not permitted to download, forward or distribute the text or part of it, without the consent of the author(s) and/or copyright holder(s), unless the work is under an open content license such as Creative Commons.

Takedown policy
Please contact us and provide details if you believe this document breaches copyrights.
We will remove access to the work immediately and investigate your claim.

This work is downloaded from Delft University of Technology.
For technical reasons the number of authors shown on this cover page is limited to a maximum of 10.

Journal of Petroleum Science and Engineering 160 (2018) 537–554

Contents lists available at ScienceDirect

Journal of Petroleum Science and Engineering

journal homepage: www.elsevier.com/locate/petrol

Multiphase transient analysis for monitoring of CO_2 flooding

Longlong Li [a,b], Denis Voskov [b,*], Jun Yao [a,**], Yang Li [c]

[a] Research Centre of Multiphase Flow in Porous Media, China University of Petroleum (East China), Qingdao 266580, China
[b] Civil Engineering & Geosciences, Delft University of Technology, Stevinweg 1, 2628 CN Delft, The Netherlands
[c] Department of Oilfield Exploration & Development, Sinopec, Beijing 100029, China

ARTICLE INFO

Keywords:
Well test analysis
CO_2 flooding
Miscibility
Corresponding analysis
Tangent line method

ABSTRACT

The potential of well test technology is discussed in this paper to estimate the miscible condition and displacement fronts position during CO_2 flooding. To interpret the multiphase well test curve of CO_2 flooding process, an accurate compositional numerical model is developed in this study. The model includes fully EoS-based compositional nonlinear formulation, unstructured gridding and multi-segmented well. A systematic well test analysis of CO_2 flooding at different regimes, including immiscible, multi-contact miscible and first-contact miscible gas injection, was performed for hydrocarbon systems with different number of components. Based on the interpretation root cause analysis, proposed in this work, the specific characteristics of the well test curve of CO_2 flooding have been identified and described. These characteristics provide the guidance for the distinction among the different regime of CO_2 displacement. It was demonstrated that the most important characteristics stay invariant from the number of components involved into numerical study. Finally, a tangent line method has been proposed to detect the key point on the pressure derivative curve corresponding to a CO_2 front. This method allows to predict the displacement front position for problems of practical interest.

1. Introduction

As a proven method for the enhanced oil recovery (EOR) (NETL, 2010; Sun et al., 2013; Kuuskraa and Koperna, 2006; Malik and Islam, 2000; Orr and Taber, 1984), the CO_2-EOR technology is becoming more and more attractive with the development of gas injection technology and increasing demand for mitigating greenhouse effect (Schneider, 1989; Nordhaus, 1991). The principle of this technology is based on the fact that the injected CO_2 can reach miscibility with the in-situ oil at reservoir conditions. During the displacement process, the mixing between the injected CO_2 and in-situ oil leads to several positive effects including oil swelling, reduction of oil viscosity and surface tension, and the evaporation of residual oil (Metcalfe and Yarborough, 1979; Holm and Josendal, 1982; Hemmati-Sarapardeh et al., 2013). All of these positive effects suggest that CO_2-EOR will play a vital role in oil recovery processes in the future (Godec et al., 2011).

However, to take full advantage of the CO_2-EOR, we need to overcome some drawbacks of this technology (Claridge and Dietrich, 1983; Moortgat, 2016; Tchelepi et al., 1993; Brock and Orr, 1991; Araktingi and Orr, 1990) which are caused by the properties of supercritical CO_2. The big difference between the mobility of CO_2 and in-situ oil can trigger viscous fingerings, and the large difference between the gas and oil densities provokes the gravity override. One of the efficient ways to overcome those negative factors is to reduce the viscosity and gravity differences by developing the miscibility between the in-situ oil and the injected gas. With the knowledge of the miscible conditions between CO_2 and oil obtained from physical or numerical experiments (Johns and Orr, 1996; Orr et al., 1993; Bretz and Orr, 1987; Jessen and Orr, 2004; Cinar et al., 2004; LaForce and Orr, 2009), it is important to know the in-situ distributions of phases during the CO_2 flooding.

But with a usual level of subsurface uncertainties, it is difficult to predict the performance of CO_2-EOR in advance. The possible solution is the continuous monitoring of CO_2 flooding process with a closed loop optimization of its performance. The potential methods to monitor the CO_2 injection process include seismic monitoring (Kendall et al., 2003; Araman et al., 2008; Terrell et al., 2002), Material Balance Equations (MBE) (Tian and Zhao, 2008) and well test. The applicability and accuracy of the seismic approach have been proved through several CO_2 injection pilot projects (Araman et al., 2008; Terrell et al., 2002; Raef et al., 2005; Davis, 2010). However, this type of monitoring is quite expensive and complex for application. The accuracy of the MBE method is constrained by too many assumptions and simplifications. The monitoring

---

* Corresponding author.
** Corresponding author.
E-mail addresses: D.V.Voskov@tudelft.nl (D. Voskov), RCOGFR_UPC@126.com (J. Yao).

https://doi.org/10.1016/j.petrol.2017.10.075
Received 5 August 2017; Received in revised form 19 October 2017; Accepted 26 October 2017
Available online 31 October 2017
0920-4105/© 2018 The Authors. Published by Elsevier B.V. This is an open access article under the CC BY-NC-ND license (http://creativecommons.org/licenses/by-nc-nd/4.0/).

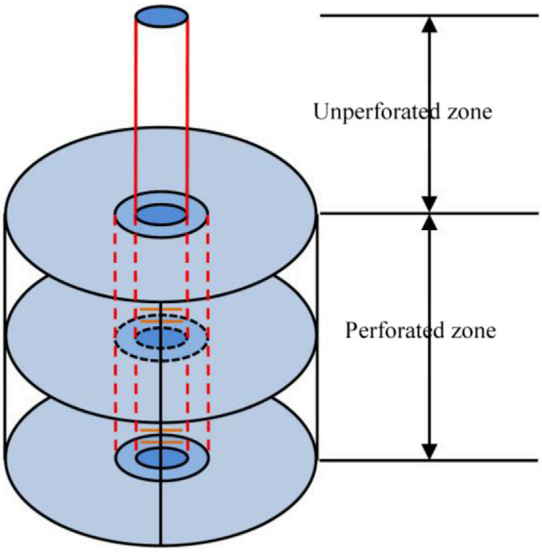

Fig. 1. The schematic of a multi-segment well model.

Table 1
Composition and component properties of simulation.

Component	Mole Fraction	P_c (bar)	T_c (K)	v_c (m^3/kg-mole)	ω	M_w (g/mol)
CO_2	0.1	73.866	304.7	0.094	0.225	44.01
C_4	0.3	37.47	419.5	0.258	0.1956	58.124
C_{10}	0.6	24.196	626	0.534	0.385	134

Table 2
Binary interaction parameters of simulation.

	CO_2	C_4	C_{10}
CO_2	0	0.1	0.1
C_4	0.1	0	0
C_{10}	0.1	0	0

Table 3
Input parameters of simulation.

Parameter	Value	Unit
Reservoir radius	300	m
Reservoir thickness	20	m
Bottom depth	400	m
Initial pressure	40	bar
Formation temperature	80	℃
Permeability	10	$10^{-3}\mu m^2$
Rock compressibility (68.9476bar)	7.2519×10^{-5}	bar^{-1}
Porosity	0.2	
Well radius	10	cm
CO_2 injection rate (surface rate)	1600	m^3/d
CO_2 injection time	1500	d

based on the well test is accurate, cheap and easy to implement.

The first attempt to make use of the well test approach is made by MacAllister (1987) which is based on a three-region composite analytical model. Then Tang and Ambastha (1988) and Su et al. (2015) developed the analytical model also based on the three-region composite model. However, the simplifications and assumptions in the analytical model limit an accurate reproduction the well test curve based on this approach. To overcome the drawbacks of the analytical model, Li et al. (2016) proposed a compositional numerical well test model which can represent the complicated miscible process. Their numerical study is focused on the inverse modeling to reproduce geological parameters, and limited by the estimation of the wellbore storage coefficient. To make full use of the response obtained from the well test, we need to reproduce the wellbore storage effect accurately and describe the particular characteristics of the well test curve related to different regimes of CO_2 displacement in detail.

In the area of the radial composite model, an extensive research has been performed in the past (Kazemi et al., 1972; Walsh et al., 1981; Satman, 1985). Based on these work, the effect of an interface on the well test curve has been studied in extensive details. However, due to the complicated mechanisms related to CO_2-EOR, it is not possible to represent the CO_2 flooding process using the radial composite model. Although it is possible to assume different compartments in the reservoir with specific displacement features, the molar fraction and corresponding phase properties, which affect the features of well test curve, cannot be assumed to remain constant in each region. Therefore, for CO_2 flooding, the interpretation method, capable to analyze the effect of the rock and fluid properties at any position on the well test curve, is required.

In this work, we employ the multi-segment well to represent the fluid flow inside the wellbore and discuss advanced gridding strategy for well test simulation. Based on the developed model, we performed a systematic interpretation of the well test curve related to CO_2 flooding process. To describe the specific characteristics of the well test curve of CO_2 flooding, we proposed a systematic analysis of the phase behavior effects in every region of the displacement profile. This analysis has been performed for the characteristics of the well test curve at typical immiscible, multiple-contact miscible and first-contact miscible CO_2 flooding. The influence of the degree of miscibility on the well test curve is observed and described in detail, which can be used for a full-field monitoring and interpretation of CO_2 flooding process. Finally, we proposed a tangent line method to detect the key point on the pressure derivative curve corresponding to the leading shock (front) of CO_2 displacement.

2. Mathematical model

Assuming only two hydrocarbon phases in the reservoir, a compositional model is applied in this study to consider the complicated mechanisms between CO_2 and in-situ oil. The compositional model is numerically solved using the Automatic Differentiation General Purpose Research Simulator (ADGPRS) (Zhou et al., 2011; Voskov, 2012; Voskov and Tchelepi, 2012).

2.1. Governing equations

Assuming n_c components in the reservoir can form two phases at thermodynamic equilibrium, the mass conservation of component i can be written as follows:

$$\frac{\partial}{\partial t}\left(\phi\sum_{j=1}^{2}x_{i,j}\rho_j S_j\right)+\nabla\cdot\sum_{j=1}^{2}x_{i,j}\rho_j\mathbf{u}_j=-\sum_{j=1}^{2}x_{i,j}\rho_j q_j\quad(i=1,\ldots,n_c)\tag{1}$$

where ϕ is the reservoir porosity; t is the time; $x_{i,j}$ is the mole fraction of component i in phase j; ρj is the phase molar density of phase j; Sj is saturation (volume fraction) of phase j; q is the source/sink term; $\mathbf{u}_j$ is the velocity of phase j:

$$\mathbf{u}_j=-\frac{kk_{rj}}{\mu_j}\nabla P\tag{2}$$

where μ is viscosity; k is the reservoir permeability; k_{rj} is the relative permeability of phase j; P is the reservoir pressure.

In the assumption of only two hydrocarbon phases, the n_c fugacity constraints describing instantaneous thermodynamic equilibrium are:

$$f_i^L=f_i^V\quad i=1,\ldots,n_c\tag{3}$$

The equation (3) can also be written as:

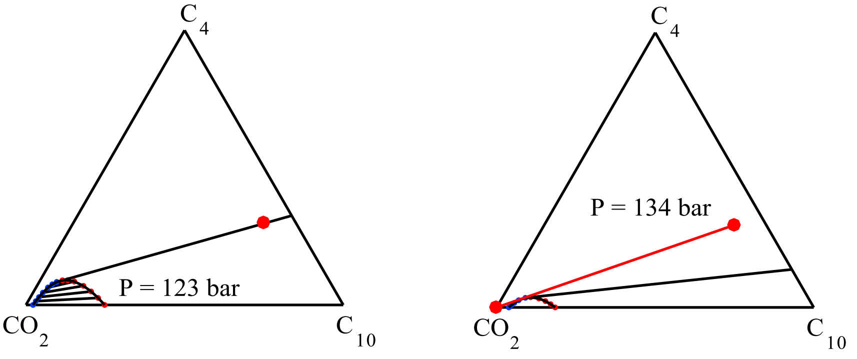

a) The ternary diagram at 123 bars

b) The ternary diagram at 134 bars

Fig. 2. The ternary diagrams.

$$\varphi_i^L x_i = \varphi_i^V y_i \tag{4}$$

where superscript *L* and *V* are phase indices for the oil and gas phases; φ is the fugacity coefficient defined as $\varphi_i = f_i / x_i p$. The details of efficient coupling of the thermodynamic solution with conservation equations, implemented in ADGPRS, see in Voskov and Tchelepi (2012) and Iranshahr et al. (2013). In addition, auxiliary relations are included to close the system:

$$\sum_{i=1}^{n_c} x_i = 1 \quad \sum_{i=1}^{n_c} y_i = 1 \quad S_o + S_g = 1 \tag{5}$$

2.2. Discretized governing equations

After meshing the physical domain, the Finite Volume Two Point Flux Approximation (TPFA) is applied to discretize the grid, the backward Euler approximation is used to discretize in time. The fully-implicit approximation of (1) can be written as:

$$\Delta t \sum_l \left(\sum_{j=1}^{2} \left(x_{i,j}^l \rho_j^l \lambda_j^l \gamma^l \Delta\psi^l \right)^{n+1} \right) + \Delta t \sum_{j=1}^{2} \left(x_{i,j} \rho_j q_j \right)^{n+1} = \left(V\phi \sum_{j=1}^{2} x_{i,j} \rho_j S_j \right)^{n+1} - \left(V\phi \sum_{j=1}^{2} x_{i,j} \rho_j S_j \right)^{n} \tag{6}$$

Here Δt is the time step; *V* is the volume of grid cell; $\Delta\psi^l$ is the potential difference over interface *l*; $\lambda_j^l = (k_{rj}/\mu_j)^l$ is the mobility of phase *j* over the interface *l* by upstream weighting; *n*+1 is the current time step; *n* is the previous time step; Υ is the transmissibility.

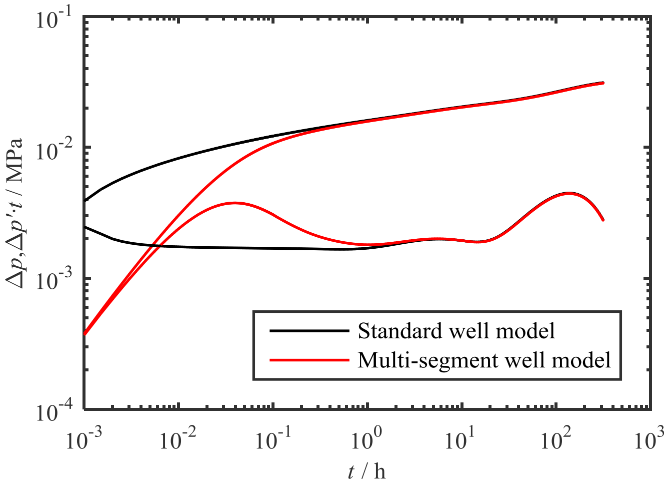

Fig. 3. The effect of the fluid flow in the wellbore on the well test curve (packer depth = 370 m).

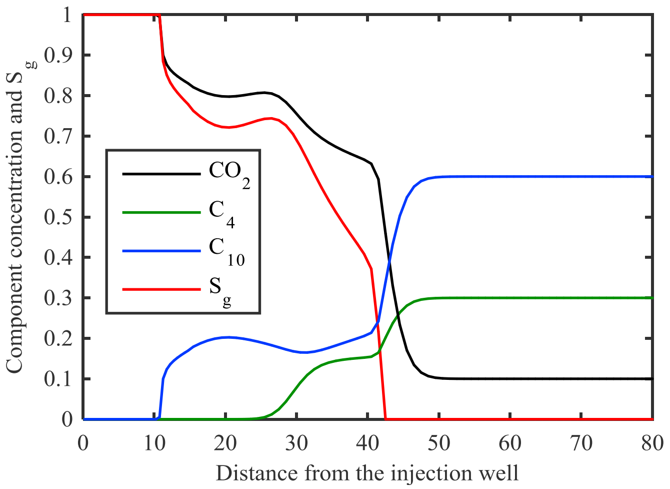

Fig. 4. The component concentration and gas saturation versus distance (in meters) from injection well.

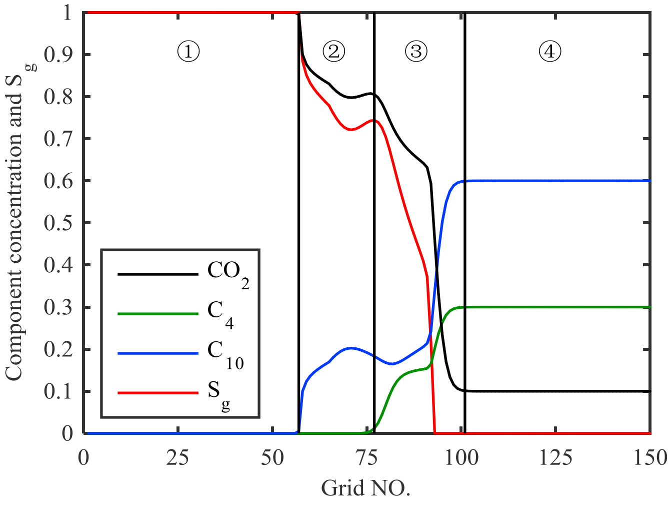

Fig. 5. The component concentration and gas saturation versus the grid-block number.

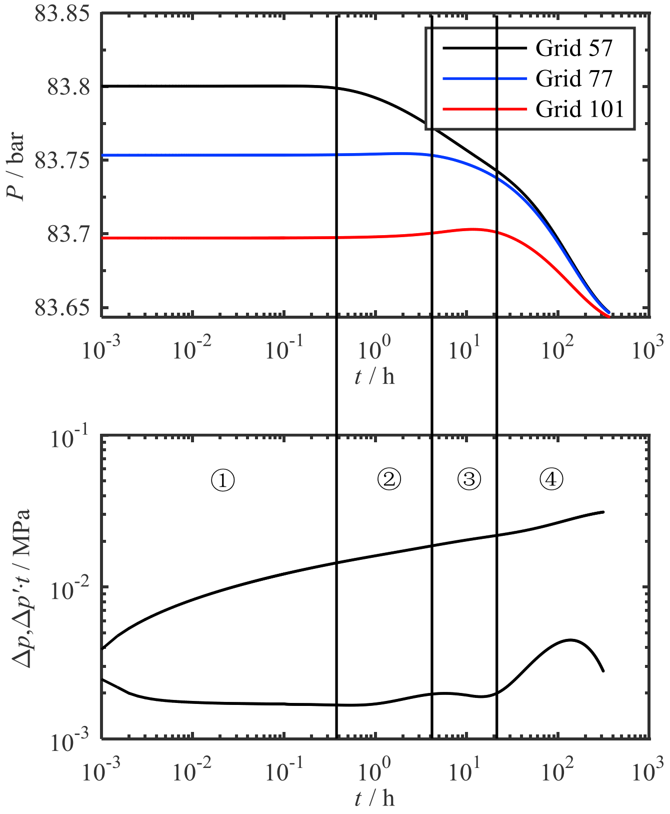

Fig. 6. Pressure and well test curve for three components hydrocarbon system at immiscible conditions.

2.3. Inner boundary model

As the flow behavior in the wellbore could be greatly affected by the phase behavior during CO$_2$ flooding, it is important to apply an accurate wellbore model to reproduce the well test curve. The well test interpretation based on the standard well model cannot resolve directly the wellbore effect, which requires an introduction of the wellbore storage coefficient used in the traditional inner boundary model of a well test (Li et al., 2016). In the case of CO$_2$ flooding, this coefficient is difficult to estimate due to the large compressibility of injection mixture. To avoid this complexity, a multi-segment well model is used in this work. As shown in Fig. 1, the well is divided into three segments, where second and third segments are connected with the reservoir through perforation intervals.

Here we adapt a multi-segment model introduced by Jiang (2008) based on an extension of the natural variable formulation for the isothermal compositional simulation. In this model, the variables for each well segment are defined as: p^w (pressure), α_j (in-situ phase fraction of phase j), $x_{i,j}$ (molar fraction of component i in phase j), the variable for each connection is defined as:

$$Q_m = A \cdot V_m. \tag{7}$$

Here, Q_m is the mixture flow rate, A is the cross-sectional area at the connection, V_m is the velocity of mixture.

The n_c mass balance equations for each node (segment) of the well are:

Table 4
The division of the reservoir.

Region NO.	1	2	3	4
Grid-block NO.	1–57	58–77	78–101	102-end

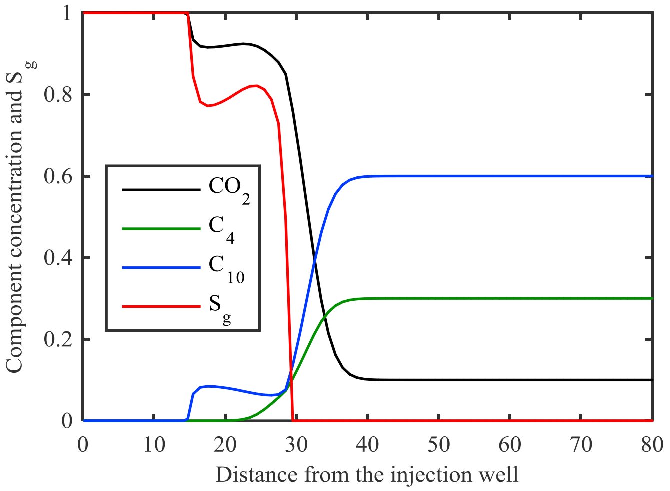

Fig. 7. The component concentration and gas saturation versus distance from injection well.

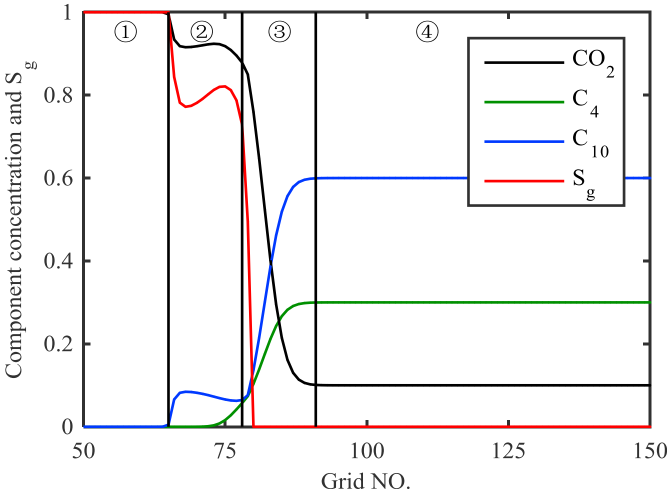

Fig. 8. The component concentration and gas saturation versus the grid-block number.

$$\frac{\partial}{\partial t}\sum_{j=1}^{2}\rho_j\alpha_j x_{i,j} - \frac{\partial}{\partial z}\sum_{j=1}^{2}\rho_j V_{sj} x_{i,j} + \sum_{j=1}^{2}\rho_j x_{i,j} q_j = 0. \tag{8}$$

Here, V_{sj} is the superficial phase velocity, q_j is the inflow of phase j to the well. In order to close the system, equation (4) is included to represent the instantaneous thermodynamic equilibrium in each segment. The constraints for the molar fractions and phase fractions can be shown as:

$$\sum_{i=1}^{n_c} x_i = 1 \quad \sum_{i=1}^{n_c} y_i = 1 \quad \sum_{j=1}^{2}\alpha_j = 1 \tag{9}$$

The homogeneous model without considering the slip, used for the CO$_2$ injection well in this work, can be described on each connection as following.

$$\Delta p^w = \Delta p_h^w + \Delta p_f^w + \Delta p_a^w \tag{10}$$

Table 5
The division of the reservoir.

Region NO.	1	2	3	4
Grid-block NO.	1–65	66–78	79–91	92-end

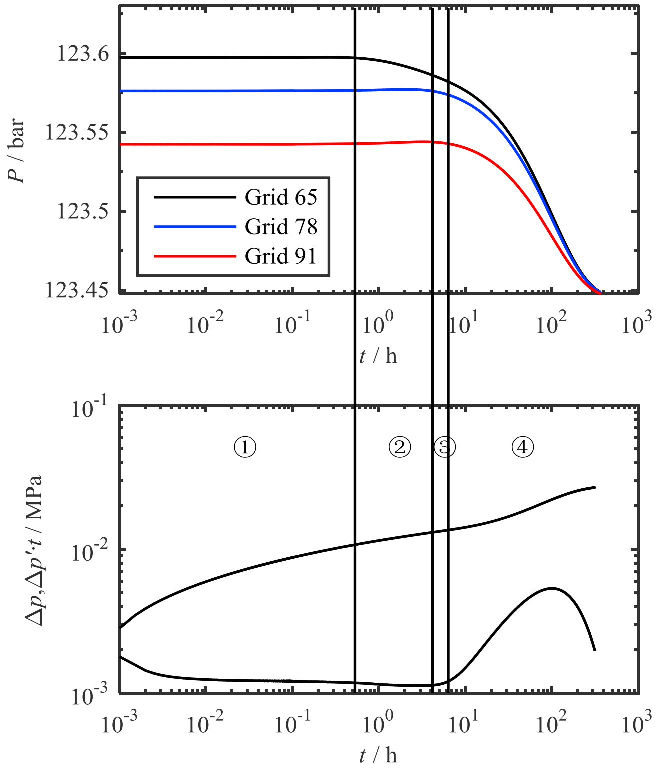

Fig. 9. Pressure and well test curve for three components hydrocarbon system at multi-contact miscible conditions.

Here Δp^w is the pressure of the segment, Δp_h^w, Δp_f^w and Δp_a^w are hydrostatic, frictional and acceleration components of pressure drop correspondingly. The drift-flux model, considered more accurate representation of multiphase flow inside the wellbore, was not applied in this work since it should not affect the results of transient analysis of CO_2 injection well.

3. Pressure transient analysis

To analyze the characteristics of the well test curve during the CO_2 flooding, falloff tests of CO_2 injection well are simulated in the radial sector model. As the well test curve of the CO_2 flooding is different from the traditional single-phase curve, the grid near the wellbore should be refined to capture the specific characteristics. Since the mechanisms of CO_2-EOR depend on the injection regime, we discuss the characteristics of well test curve at three typical conditions: immiscible, multi-contact miscible and first-contact miscible.

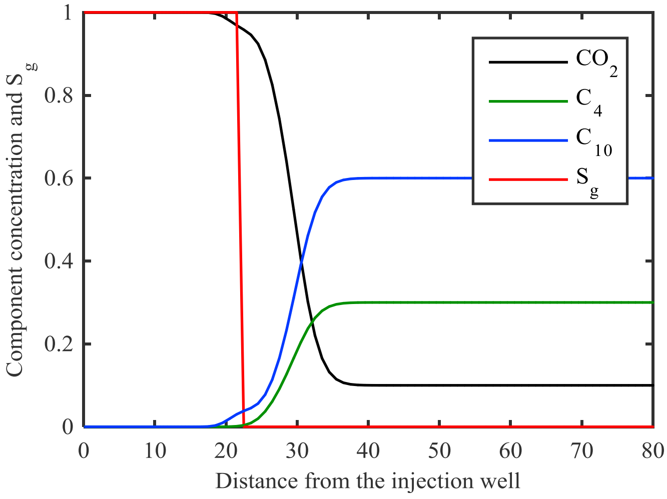

Fig. 10. The component concentration and gas saturation versus distance from injection well.

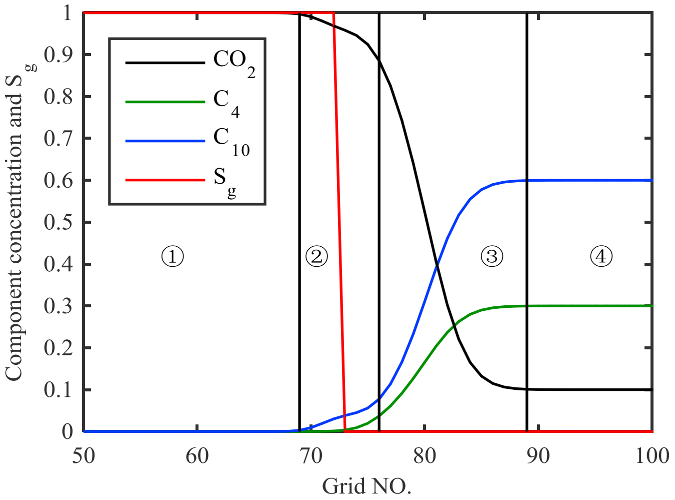

Fig. 11. The component concentration and gas saturation versus the grid-block number.

Table 6
The division of the reservoir.

Region NO.	1	2	3	4
Grid-block NO.	1–69	70–76	77–89	90-end

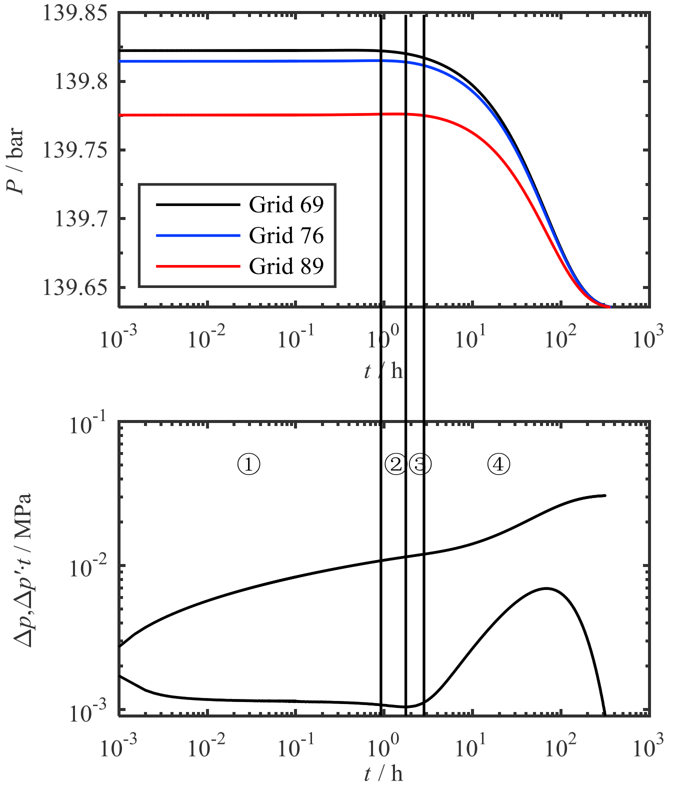

Fig. 12. Pressure and well test curve for three components hydrocarbon system at first-contact miscible conditions.

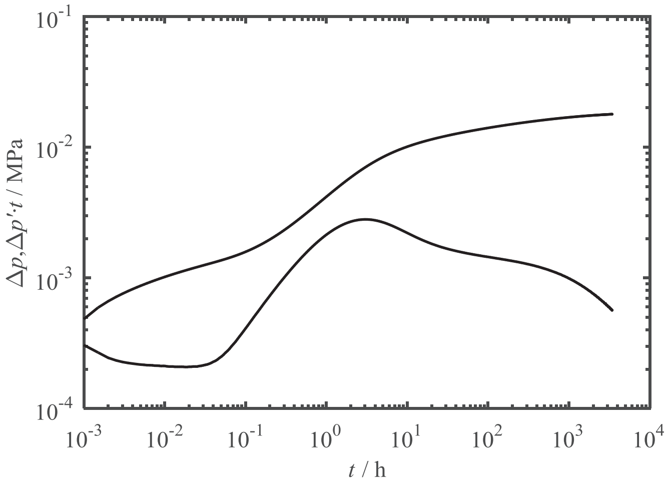

Fig. 13. The well test curve with radial flow of in-situ oil region.

Table 7
Composition and component properties of simulation.

Component	Mole Fraction	P_c (bar)	T_c (K)	v_c (m^3/kg-mole)	ω	M_w (g/mol)
CO_2	0.01	73.866	304.7	0.094	0.225	44.01
C_1	0.2	46.042	190.60	0.098	0.013	16.043
C_4	0.24	37.47	419.5	0.258	0.1956	58.124
C_{10}	0.55	24.196	626	0.534	0.385	134

Table 8
Binary interaction parameters of simulation.

	CO_2	C_1	C_4	C_{10}
CO_2	0	0.1	0.1	0.1
C_1	0.1	0	0	0.04092
C_4	0.1	0	0	0
C_{10}	0.1	0.04092	0	0

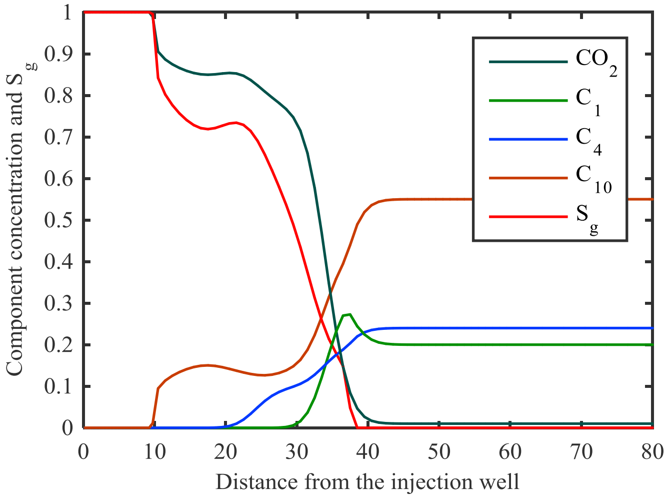

Fig. 14. The component concentration and gas saturation versus the distance from injection well.

3.1. Three components hydrocarbon system

A three components hydrocarbon system is used in this section. The composition, component properties and binary interaction parameters of the oil are shown in Tables 1 and 2, with the input parameters of the simulation shown in Table 3. The radial grid was generated using the following scheme [0.1:0.1:1, 1:0.2:10, 10:0.5:15, 15:1:25, 25:1:40, 40:1:60, 60:1:300], where 15:1:25 corresponds to mesh changes between $r = 15$ m to $r = 25$ m with step $\Delta r = 1$ m. The ternary diagrams at 123 bars

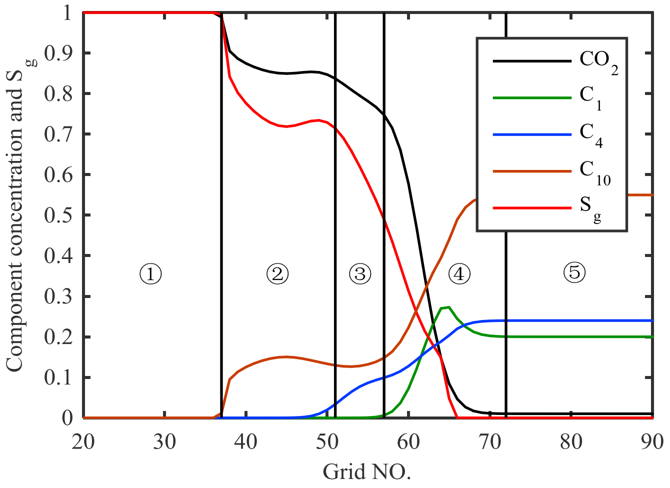

Fig. 15. The component concentration and gas saturation versus the grid-block number.

Table 9
The division of the reservoir.

Region NO.	1	2	3	4	5
Grid-block NO.	1–37	38–51	52–57	58–72	73-end

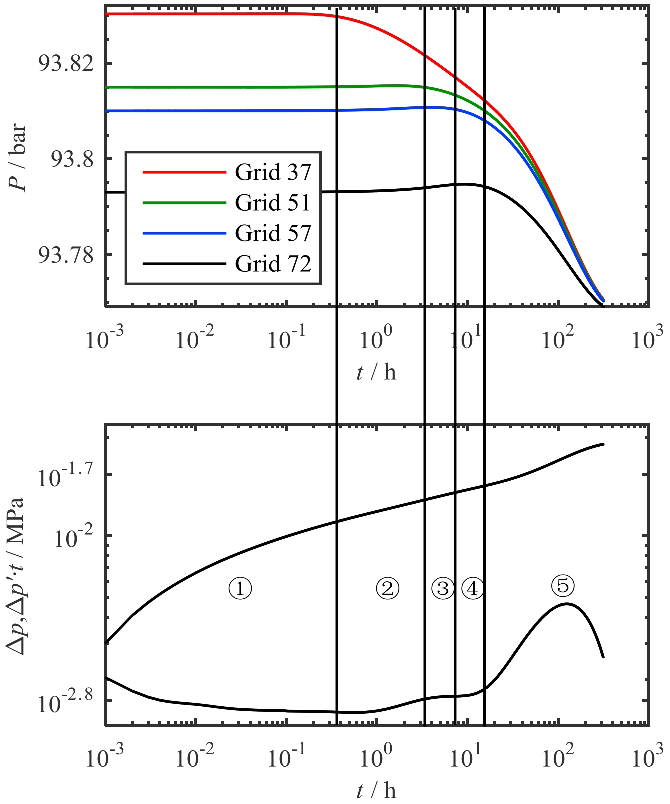

Fig. 16. Pressure and well test curve for four components hydrocarbon system at immiscible conditions.

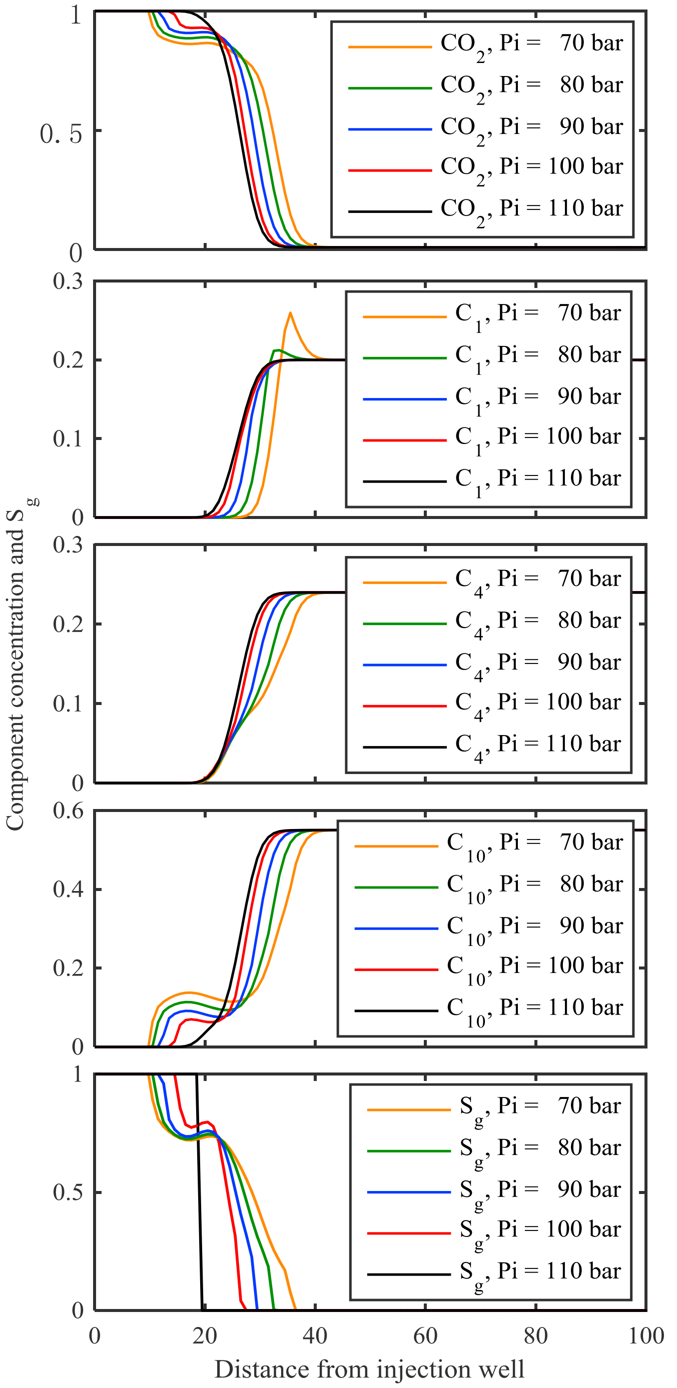

Fig. 17. The component concentration and gas saturation versus distance from injection well at different miscible conditions.

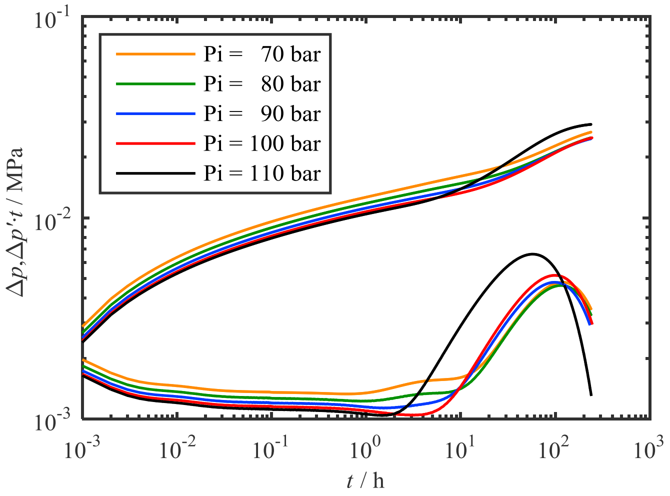

Fig. 18. The well test curves at different miscible conditions.

and 134 bars are shown in Fig. 2, based on which, we can control the miscibility underground by controlling the injection strategy.

The wellbore storage effect can be represented accurately by applying the multi-segment well model. However, as it is shown in Fig. 3, the characteristics of the well test curve are covered by the wellbore storage effect in the early flow regime. To focus on the characteristics of the well test curve corresponding to the near-well reservoir, we can neglect the effect of wellbore storage and will apply the standard well model in the following analysis. The pressure derivative curve mainly reflects the rock and fluid properties in the reservoir, especially the fluid mobility. In other words, the component composition and gas saturation, which determine the mobility distribution, have a large effect on the well test curve. We propose the following method to analyze the effect of the component composition and gas saturation distribution on the well test curve.

The procedure of corresponding analysis contains several steps. First, we align the x-coordinate with well test curve and draw the pressure variation at specific position after well shut-in, see Fig. 6 for example. Next, we associate the time when the pressure at a particular position in space begins to decrease with the time when the mobility begins to affect the well test curve (see Appendix for derivations supporting this observation). Finally, evaluating the fluid and rock properties in the numerical simulation process, we can trace the effect of property changes on the well test curve. Note that the proposed approach can be used to interpret the effect of fluid properties in every block or at any position on the well test curve.

3.1.1. Immiscible flooding

First, we start our analysis from a purely immiscible gas injection. Fig. 4 and Fig. 5 show the component concentration and gas saturation versus the distance from the injection well and the grid-block number respectively. Based on Fig. 5, the reservoir is divided into 4 regions (Table 4) typical for immiscible displacement. By using the corresponding analysis method for grid-blocks 57, 77 and 101 shown in Fig. 6, we can divide the well test curve into 4 regimes. The characteristics of well test curves in all 4 regions of immiscible displacement solution will be discussed in detail below. Here, we are not using a composite model to interpret the well test curve of CO_2 flooding. The fluid properties are not constant in specified regions and the changes of molar fraction and phase properties are considered at every point of the reservoir.

***Regime* 1**: the pressure derivative curve in this flow regime goes downward at the beginning and then becomes flat. We can point to two reasons which lead the pressure derivative curve downward: first, the shut-in well event during simulation results in a large variation of the bottom hole pressure in a very short time; second, the mean mobility of the pressure wave propagated zone caused by shut-in well will increase due to the facts that gas viscosity reduces with decreasing pressure, and the mean pressure of the propagated zone decreases with time. Since only a single-phase gas exists in the first region (blocks from 1 to 57), the pressure derivative curve is stabilized and becomes flat when the reservoir is homogeneous and the area of this zone is large enough.

***Regime* 2**: the pressure derivative curve in this flow regime goes upward. In Fig. 5 you can see a C_{10} bank and no C_4 in the region from grid-block 58 to 77, which is a consequence of vaporizing displacement.

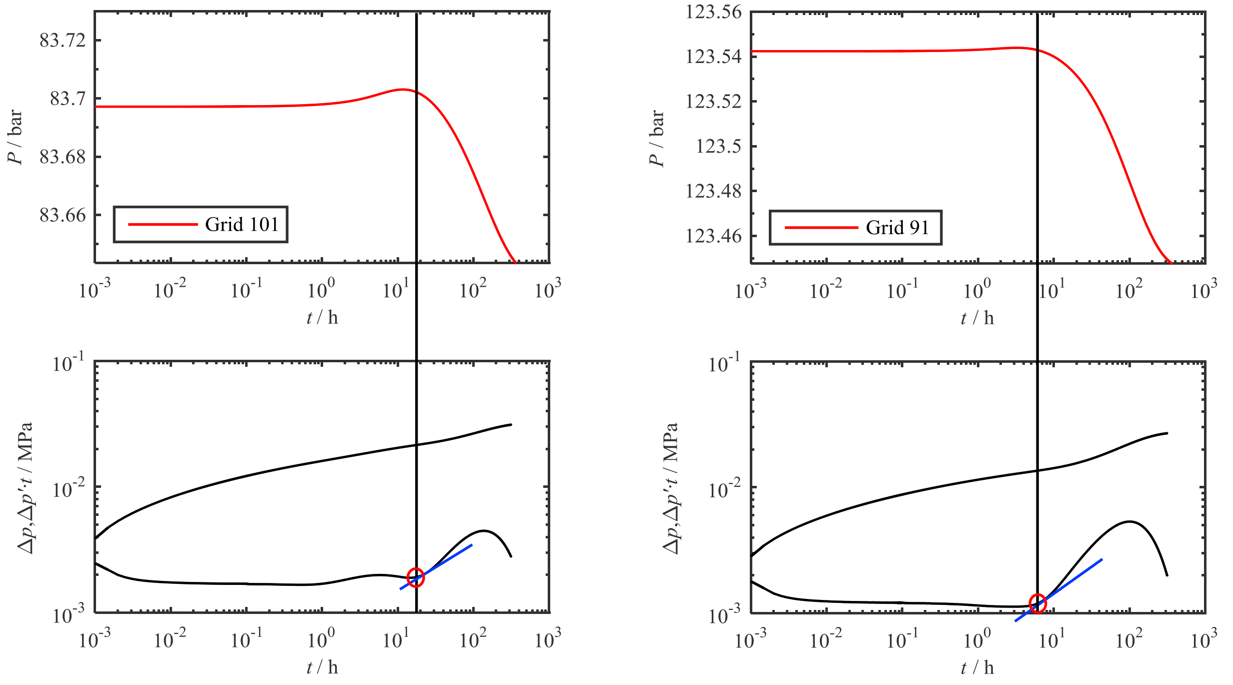

a) Immiscibility

b) Multiple-contact miscibility

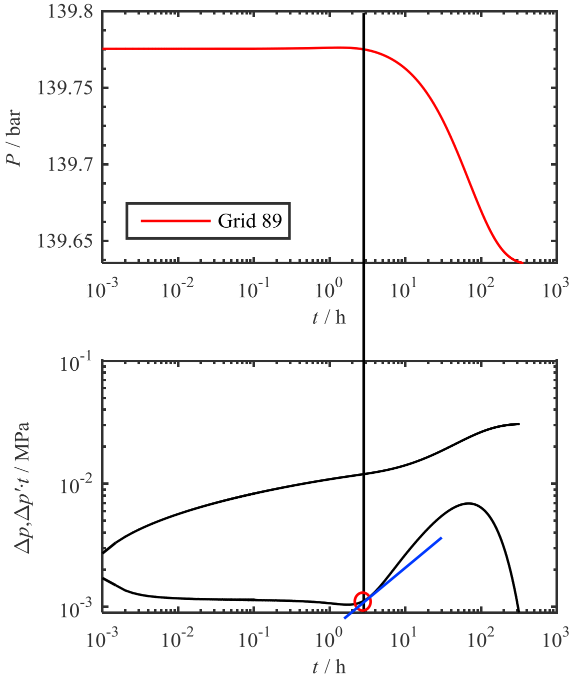

c) First-contact miscibility

Fig. 19. Tangent line method to detect the frontal point (3 components system).

The phase behavior in this region is mainly determined by CO_2-C_{10} binary mixture. Compared with region 1, the existence of C_{10} bank will lead to the more significant reduction of CO_2 concentration and gas saturation which will result in mobility reduction. Although there is a slight reduction in C_{10} and increase in CO_2 concentration in the end, it will not affect the fluid mobility a lot. Therefore, the regions 1 and 2 can be represented as a composite reservoir model, which can be simplified as the pure CO_2 region and C_{10} bank region. In the literature on composite well test models (Ambastha, 1989, 1995), it is shown that the well test curve characteristics of composite model will be controlled by two factors:

$$M = \frac{(k/\mu)_1}{(k/\mu)_2} \quad F_s = \frac{(\phi c_t)_1}{(\phi c_t)_2} \tag{11}$$

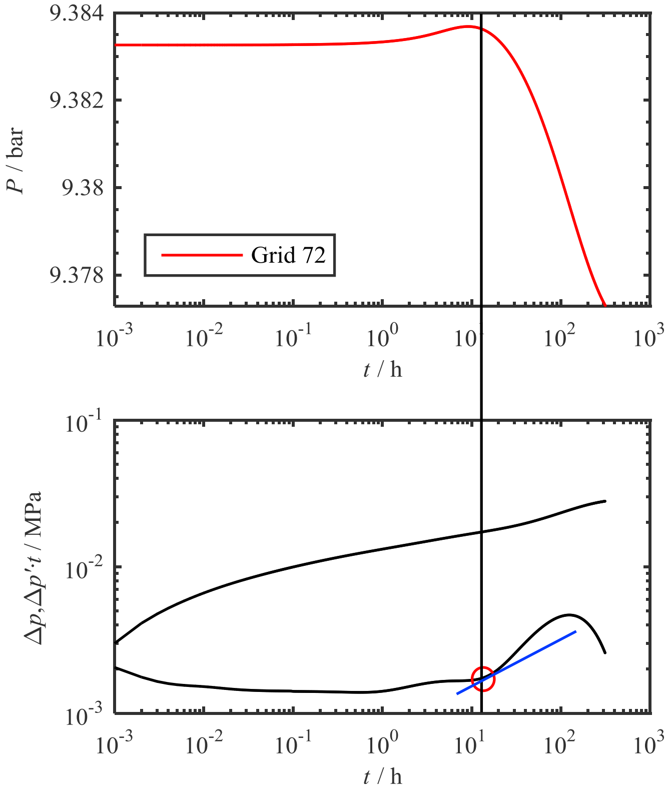

Fig. 20. Tangent line method to detect the frontal point (4 components system).

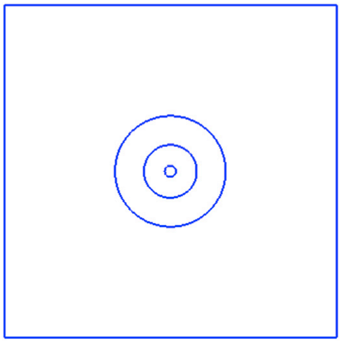

Fig. 21. The geometric model.

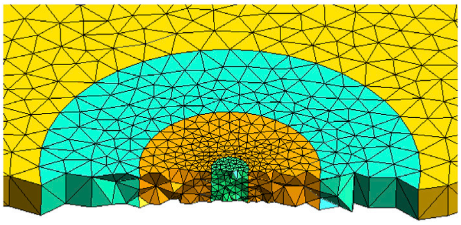

Fig. 22. The discretized model.

where c_t is the total compressibility, and the subscripts 1 and 2 represent the pure CO_2 and C_{10} bank regions.

Here, the values of M and F_s are larger than unity, which will lead to the pressure derivative curve rise first, then fall and become flat. Since the area of C_{10} bank is not large enough in our solution, the last two characteristics didn't appear. As a result, the pressure derivative curve in this flow regime moves upward. Due to the low C_{10} concentration and high CO_2 concentration in the first few grid-blocks, the upward degree of the derivative curve is very low in the beginning.

Regime **3**: the pressure derivative curve moves downward first and then rises. From grid-blocks 78 to 101, there is a C_4 bank and the phase behavior is dependent on CO_2, C_4 and C_{10}. From Fig. 5, the decreasing CO_2 and increasing C_4 and C_{10} will lead to a sharp reduction of gas saturation in the reservoir. Then, the decreasing mobility makes this region an extension of region 2. The disappeared trends for a composite model in regime 2, of which the derivative curve falls and becomes stable, can be observed in this regime. But since the mobility of region 3 is lower than region 2, the pressure derivative will not stabilize in practice, it will go upward in the end because of the decreasing mobility.

Regime **4**: the pressure derivative curve in this flow regime turns upward. From grid-block 102 to the last grid-block, there is no existence of CO_2 which leads to a lower mobility of region 4 than region 1–3. Therefore, the pressure derivative curve will go upward.

3.1.2. Multi-contact miscible flooding

With the increase of pressure, the two-phase region on the ternary diagram will shrink, see Fig. 2 for example. The leading shock, connecting the initial composition, will be distributed along the critical tie-line which makes the displacement a multi-contact miscible. In the simulation below, we keep pressure slightly above the minimum miscible pressure (MMP) to control miscibility. Note that the displacement efficiency improves drastically when approaching miscible conditions.

In this section, we change the initial reservoir pressure to 92 bars which help us to reach a multi-contact miscible condition with the in-situ oil. Fig. 7 and Fig. 8 show the component concentration and gas saturation versus the distance from the injection well and the grid-block number respectively. Based on Fig. 8, the reservoir is divided into 4 regions, see Table 5. Similar to immiscible displacement, we used the corresponding analysis method for grid-blocks 65, 78 and 91 and again divide the well test curve into 4 regimes (see Fig. 9).

Regime **1**: the pressure derivative curve in this flow regime goes downward at the beginning and then becomes stable. The characteristics are quite similar to the 1st regime at the immiscible condition which helps to apply similar interpretations.

Regime **2**: the pressure derivative curve in this flow regime falls slightly. Even though the component concentration and gas saturation in this regime look similar to the 2nd regime at immiscible flooding, the C_{10} concentration is much lower at multi-contact miscible conditions which lead to a higher gas saturation. Therefore, the mobility and storability differences between regions 1 and 2 are very small at multi-contact miscible conditions. Thus, the derivative curve has a potential trend to turn upward slightly. But as we mentioned before, the gas phase mobility of the pressure wave propagated zone will increase with decreasing pressure, and now regions 1 and 2 contain more gas phase which leads to another potential trend that the derivative curve turns downward. Between these two converse trends, the second is prevailing which forces the pressure derivative curve fall slightly in this regime.

Regime **3**: the pressure derivative curve moves upward. Compared with the immiscibility condition, the C_4 bank disappears, the component concentrations change quickly and the gas saturation reduces to zero very fast. Therefore, this flow region at multi-contact miscible conditions significantly shrinks.

Regime **4**: the pressure derivative curve in this flow regime turns upward by the same reason as in immiscibility condition.

With the development of the miscibility, the regime 1 moves backward and the regime 4 moves forward on the well test curve which means that the pure CO_2 region becomes larger, the mixing region becomes smaller and the displacement efficiency improves.

3.1.3. First-contact miscible flooding

When the pressure is high enough, the displacement trajectory is reduced to the dilution line, which connects the injection and initial

Table 10
Composition and component properties of simulation.

Component	Mole Fraction	P_c (bar)	T_c (K)	v_c (m^3/kg-mole)	ω	M_w (g/mol)
CO_2	0.000436	73.866	304.7	0.094	0.225	44.01
C_1	0.27215	46.042	190.6	0.098	0.013	16.043
C_2	0.004128	48.839	305.43	0.148	0.0986	30.07
C_3	0.010484	42.455	369.8	0.2	0.1524	44.097
NC_4	0.02123	37.966	425.2	0.255	0.201	58.124
NC_5	0.02002	33.701	469.6	0.311	0.251	72.151
C_6	0.022566	30.104	507.5	0.351	0.299	84
C_7-C_9	0.098746	28.641	577.9389	0.51936	0.3165	145.16
C_{10}-C_{13}	0.10053	17.609	666.4667	0.78898	0.4255	223.26
C_{14}-C_{19}	0.14514	14.059	748.0889	1.2107	0.5768	353.51
C_{20}-C_{35}	0.16416	10.896	851.5389	1.8931	0.7659	554.55
C_{36+}	0.14041	6.5363	1092.983	3.7472	1.1313	1052

Table 11
Binary interaction parameters of simulation.

	CO_2	C_1	C_2	C_3	NC_4	NC_5	C_6	C_7-C_9	C_{10}-C_{13}	C_{14}-C_{19}	C_{20}-C_{35}	C_{36+}
CO_2	0	0.1	0.1	0.1	0.1	0.1	0.1	0.1	0.1	0.1	0.1	0.1
C_1	0.1	0	0	0	0	0	0.0279	0.042242	0.049554	0.05624	0.061891	0.0717
C_2	0.1	0	0	0	0	0	0.01	0.01	0.01	0.01	0.01	0.01
C_3	0.1	0	0	0	0	0	0.01	0.01	0.01	0.01	0.01	0.01
NC_4	0.1	0	0	0	0	0	0	0	0	0	0	0
NC_5	0.1	0	0	0	0	0	0	0	0	0	0	0
C_6	0.1	0.0279	0.01	0.01	0	0	0	0	0	0	0	0
C_7-C_9	0.1	0.042242	0.01	0.01	0	0	0	0	0	0	0	0
C_{10}-C_{13}	0.1	0.049554	0.01	0.01	0	0	0	0	0	0	0	0
C_{14}-C_{19}	0.1	0.05624	0.01	0.01	0	0	0	0	0	0	0	0
C_{20}-C_{35}	0.1	0.061891	0.01	0.01	0	0	0	0	0	0	0	0
C_{36+}	0.1	0.0717	0.01	0.01	0	0	0	0	0	0	0	0

Table 12
Input parameters of simulation.

Parameter	Value	Unit
Reservoir size	600 × 600	m
Reservoir thickness	20	m
Bottom depth	1000	m
Initial pressure	100	bar
Formation temperature	80	°C
Permeability	10	mD
Rock compressibility (68.9476bar)	7.2519×10^{-5}	bar^{-1}
Porosity	0.2	
Well radius	10	cm
CO_2 injection rate (surface rate)	3000	m^3/d
CO_2 injection time	200	d

composition and not passing through the two-phase region (see Fig. 2,b for example). At this condition, the displacement efficiency reaches almost 100% which indicates the first-contact miscible condition. In this section, we change the initial reservoir pressure to 110 bars and describe characteristics of well test curve at the first-contact miscible conditions. Fig. 10 and Fig. 11 show the component concentration and gas saturation versus the distance from the injection well and the grid-block number respectively. Based on Fig. 11, the reservoir is divided again into 4 regions, see Table 6.

As shown in Fig. 12, the characteristics of the well test curve are similar to the multi-contact miscibility condition. But the time interval of regimes 2 and 3 shrink significantly in comparison with the immiscible or multi-contact miscible conditions. This indicates that the mixing region is very small and the displacement is almost piston-like which are the main characteristics of the first-contact miscible flooding.

In conclusion, we can distinguish the immiscible and miscible conditions by using the shape of pressure derivative curve and estimate the degree of miscibility by measuring the length of the time interval of regimes 2 and 3. The length of the time interval of regime 3 reduces significantly when the displacement is changing from immiscible to multi-contact miscible conditions, but it is not changing a lot from multi-contact to first-contact miscible conditions. The length of the time interval of regime 2 reduces for both types of miscibility.

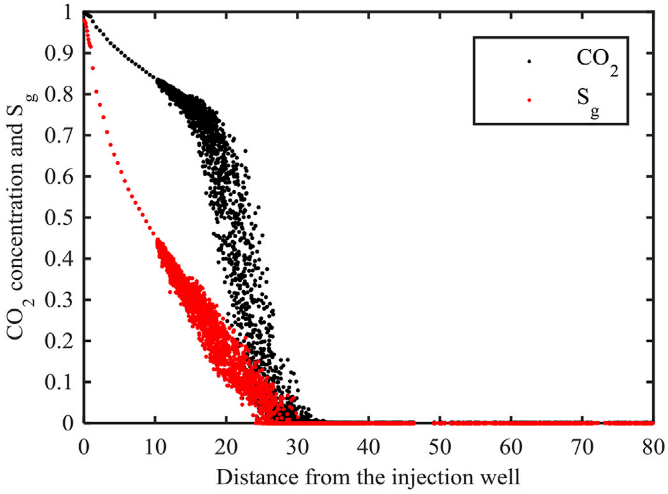

Fig. 23. The CO_2 concentration and gas saturation distribution versus distance from injection well.

When the reservoir dimensions are large, we can observe the radial flow regime corresponding to an in-situ oil region. As shown in Fig. 13, this regime can significantly affect the pressure derivative curve. However, in our study, we focus on the pressure response of CO_2 swept region and therefore, we will not discuss the radial flow regime corresponding to the in-situ oil region.

3.2. *Four components hydrocarbon system*

In this section, we investigate major characteristics of well test curve for a typical four components hydrocarbon mixture. The initial

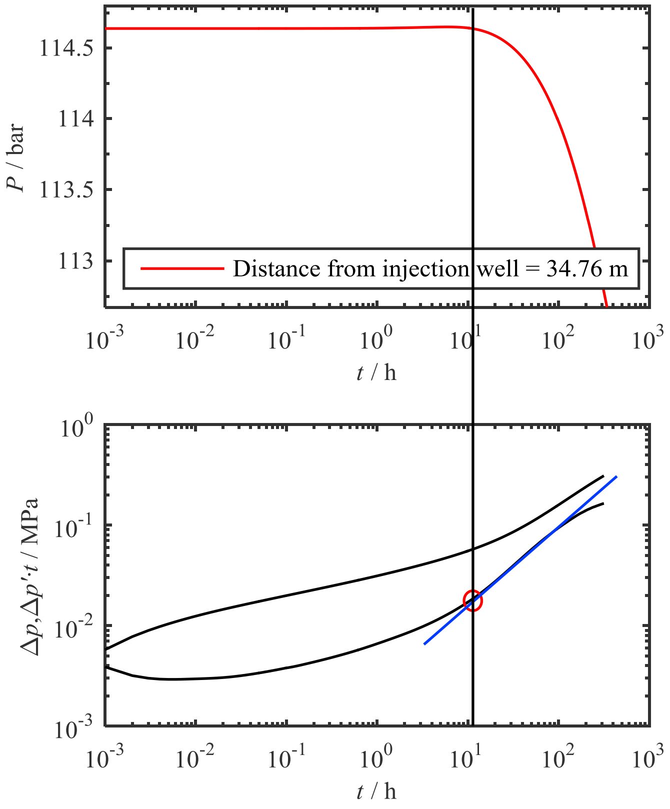

Fig. 24. Tangent line method to detect the frontal point (12 components system).

composition, component properties and binary interaction parameters of the oil are shown in Tables 7 and 8. In this study, we use the same simulation parameters described in Table 3, except that the formation temperature is equal to 345 K and initial reservoir pressure is equal to 65 bars. The injection of pure CO_2 at these conditions provides an immiscible displacement regime. In addition, the same system can be used to achieve different miscible regimes including condensing-vaporizing gas drive (Orr et al., 1993). The radial grid was constructed using the following grid-block distributions: [0.1:0.05:1, 1:0.5:10, 10:1:15, 15:1:25, 25:1:40, 40:1:60, 60:3:300].

Fig. 14 and Fig. 15 show concentrations and gas saturation versus the distance from injection well and the grid-block number respectively. Based on Fig. 15, the reservoir is divided into 5 regions (Table 9). The corresponding analysis method was applied again for grid-blocks 37, 51, 57 and 72 the well test curve was divided into 5 regimes (see Fig. 16).

By using the corresponding analysis method for grid-blocks 37, 51, 57 and 72 shown in Fig. 15, we can divide the well test curve into 5 regimes. The characteristics of well test curve are discussed in details at immiscible conditions.

***Regime* 1**: the pressure derivative curve goes downward at the beginning, and then becomes stable. The characteristics are similar to the three components system described in section 3.1.

***Regime* 2**: the pressure derivative curve in this flow regime goes upward. As shown in Fig. 15, there is a C_{10} bank in the region 2 and almost no presence of C_1 and C_4, which is related to the vaporizing displacement. The phase behavior in this region is mainly determined by CO_2 and C_{10}. The description of well test curve characteristics is similar to the 2nd flow regime of three component system at immiscible condition.

***Regime* 3**: the pressure derivative curve goes upward with a lower slope than regime 2. In this region, C_1 disappeared from in-situ oil, and the phase behavior depends on interactions among CO_2, C_4 and C_{10}. It is clear from Fig. 15 that the reduction of CO_2 and increase of C_4 and C_{10} will lead to a sharp reduction of gas saturation in the reservoir. The explanation proposed for the 3rd regime with three components system at immiscible condition can be applied here to describe the characteristic of pressure derivative curve.

***Regime* 4**: the pressure derivative curve goes upward. The well test curve in this flow regime is mainly affected by the grid-blocks in the range 58–72. In this region, the increase of C_4 and C_{10} leads to the reduction of gas saturation. At the immiscibility condition, the mobility difference between gas and oil phases is larger than multi-contact and first-contact miscibility conditions. Therefore, the effect of gas saturation variation on the mobility and on well test curve is stronger than the gas phase mobility variation caused by pressure drop. Although the gas saturation decreases with increasing C_4 and C_{10}, the existence of C_1 bank, which can be interpreted as a condensing displacement, will improve the phase properties even for the gas phase. As a result, the pressure derivative curve begins to go upward with a low slope.

***Regime* 5**: the pressure derivative curve in this flow regime turns upward. The reason of this characteristic is the same as the 4th flow regime of three component system at immiscibility condition.

Based on the pressure transient analysis above, we can conclude that the characteristics of well test curves of three and four component systems are similar. Therefore, we can divide the well test curve of CO_2 flooding in general case of multicomponent mixture into four flow regimes: first flow regime corresponding to pure CO_2 region, second flow regime corresponding to heavy hydrocarbon bank, third flow regime corresponding to medium and light hydrocarbon bank, and fourth flow regime corresponding to in-situ oil region. Notice that the four flow regimes and regions used for the analysis of well test curve here are different from the composite model where all properties are constant in each region.

By increasing the reservoir pressure, we can develop miscibility in the reservoir. As shown in Fig. 17, with the increasing pressure, the leading and trailing shocks are getting closer which means a higher miscibility degree. We can observe the characteristics of well test curve at different degree of miscibility shown in Fig. 18. On pressure derivative curve, the relative position of the segment corresponding to two-phase region, will move downward and shrink with the development of miscibility. The segment corresponding to pure CO_2 region will move backward, and the segment corresponding to CO_2 un-swept region will move forward.

Therefore, we can generate well test curves at different miscible conditions with numerical simulation approach used in this paper, and then estimate the degree of miscibility by comparing the real well test curve with the numerical one. Finally, with the estimation of the in-situ miscible conditions, it becomes easier to determine the displacement efficiency of CO_2 injection, and optimize the reservoir operations correspondingly.

4. A tangent line method to detect the frontal point

The important function of the well test curve is to estimate the character of processes in the reservoir. One of the important characteristics of CO_2 flooding is the position of the front (leading shock). Therefore, the important interpretation of multi-phase well test is to detect the point on the pressure derivative curve corresponding to the CO_2 front. Based on that, the segment on the well test curve corresponding to the CO_2 swept region can be specifically analyzed. Since interactions between CO_2 and in-situ oil in the gas injection process is rather complex, the form of the well test curve is different from the traditional single-phase flow process.

Based on the pressure transient analysis performed above, we can identify the CO_2 front on the pressure derivative curve. Then, by observing these frontal positions in Fig. 19 and Fig. 20, we summarize a tangent line method. The method contains several steps: first, find the time interval on the pressure derivative curve corresponding to the original oil region (un-swept by CO_2); next, draw a tangent line of the pressure derivative curve in the early segment of this time interval; the frontal intersection between the tangent line and the pressure derivative curve is the key point corresponding to the CO_2 front. This approach is based on the fact that the mobility of the original oil region is lower than the mobility in CO_2 swept region, which makes the pressure derivative curve move upward with a higher slope.

We tested the proposed tangent line method for a more complicated hydrocarbon system in a realistic reservoir model. The homogeneous 3D model is shown in Fig. 21. We used the Gmsh (Geuzaine and Remacle, 2009), a three-dimensional unstructured mesh generator, to discretize the reservoir model. The discretized model is shown in Fig. 22, based on which we applied a specifically designed meshing strategy (see Appendix B) to obtain accurate solutions. A typical hydrocarbon system with 12 components is taken from Eclipse PVTI Tutorials (Eclipse Technical Description, 2006). The initial composition, component properties and binary interaction parameters of the initial oil mixture are described in Tables 10 and 11, the input parameters of the simulation are shown in Table 12.

This simulation is performed at immiscible conditions which is clear from the CO_2 concentration and gas saturation profiles shown in Fig. 23. Here we apply the tangent line method to estimate the frontal point and compare it with the position of the displacement front in numerical solution. The displacement front based on the tangent line method is predicted at 34.76 m as shown in Fig. 24 which is close to the position of displacement front in Fig. 23.

5. Conclusions

A compositional numerical well test model, which can reproduce the well test curve for multiphase system accurately, is presented in this work to analyze the characteristics of well test curve during CO_2 flooding. Due to the complicated mechanisms of CO_2-EOR, the phase behavior and component interactions during CO_2 flooding lead to specific characteristics of the well test curve. To understand these characteristics, a corresponding multiphase pressure transient analysis is proposed in this paper to interpret the corresponding displacement regions on a well test curve. The well test curve has been analyzed at immiscible, multiple-contact miscible and first-contact miscible conditions. The effect of the development of miscibility on the well test curve is discussed in details which are useful for interpretation of well test curve of CO_2 flooding in practical applications. Based on the corresponding analysis, a tangent line method is proposed to detect the frontal point on the typical well test curve which can be used for monitoring of the CO_2 flooding process. As the reservoir conditions and corresponding hydrocarbon system cannot be specified or reduced to several simulated scenarios in practice, the characteristics of well test curve of CO_2 flooding may not always contain particular sequence of regions observed in our work. However, the proposed analysis makes it easy to interpret the characteristics of the well test curve for practical CO_2 flooding processes and identify the position of the displacement front.

Acknowledgements

We would like to thank the China Scholarship Council for supporting our work. We also thank the Stanford University Petroleum Research Institute for Reservoir Simulation (SUPRI-B) program for the permission to use ADGPRS in this work.

Nomenclature

f	Fugacity of component in oil or gas phase [10^{-1}MPa]
k	Absolute permeability [μm^2]
k_r	Relative permeability of phases [−]
n_c	Total number of hydrocarbon components [−]
P	Reservoir pressure [10^{-1}MPa]
q	Sink/source per unit volume of reservoir [$mol/cm^3/s$]
S	Saturation of water, oil or gas phase [−]
t	Time [s]
V	Volume [cm^3]
$\mathbf{u}$	Darcy velocity of oil or gas phase [cm/s]
x	Molar fraction in oil phase [−]
y	Molar fraction in gas phase [−]
φ	Fugacity coefficient [−]
ϕ	Reservoir porosity [−]
ρ	Molar density of oil or gas phase [mol/cm^3]
μ	Viscosity [cP]
λ	Phase mobility [cP^{-1}]

Subscripts

g	Gas phase
i	Index of mass component
o	Oil phase

Superscripts

n	Time step level

Appendix A

The government equation of single phase radial flow can be written as:

$$\frac{1}{r}\frac{\partial}{\partial r}\left(r\frac{\partial P}{\partial r}\right) = \frac{\phi\mu c_t}{k}\frac{\partial P}{\partial t} \tag{12}$$

where r is the radius, c_t is the total compressibility, t is the injection time. The boundary and initial conditions are:

$$\begin{aligned} &P = P_i \quad at \quad t = 0 \\ &P = P_i \quad at \quad r = \infty \\ &\lim_{r \to 0} r\frac{\partial P}{\partial r} = \frac{q\mu}{2\pi kh} \quad at \quad t > 0 \end{aligned} \tag{13}$$

By solving these equations, we can obtain the solution below:

$$P_{r,t} = P_i - \frac{q\mu}{4\pi kh}\int_{X=\frac{\phi\mu c_t r^2}{4kt}}^{\infty}\frac{e^{-s}}{s}ds = P_i - \frac{q\mu}{4\pi kh}\mathrm{ei}(X) \quad X = \frac{\phi\mu c_t r^2}{4kt} \tag{14}$$

The pressure solution of falloff test can be solved with the application of superposition theorem. The schematic of this method in Fig. 25 shows that the solution with injection/production history in Fig. 25 (a) is equivalent to the combined solution of two wells with inverse injection/production rate in Fig. 25 (b).

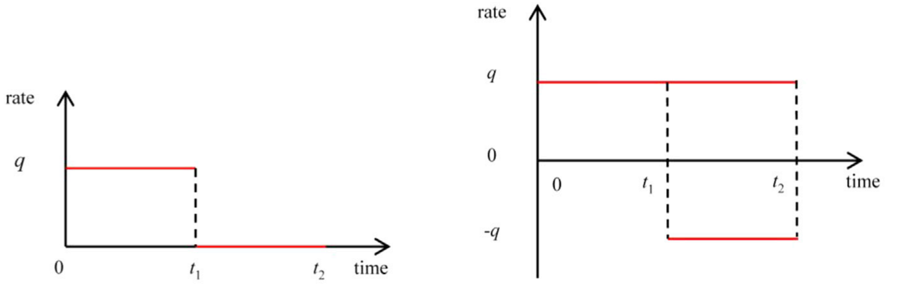

a) Original rate vs time b) Two rates vs time with application of superposition theorem

Fig. 25. The schematic of the superposition theorem for falloff test.

By combining two solutions obtained with rate q at $t = [0, t_2]$ and rate $-q$ at $t = [t_1, t_2]$, the pressure solution during falloff test can be presented as:

$$P_i - P(r,t) = [P_i - P(r, t_1 + \Delta t)] - [P_i - P(r, \Delta t)] \quad \Delta t = t - t_1 \tag{15}$$

From equation (14), the pressure at distance r will be controlled by rate q at $t = [0, t_2]$ before the pressure wave caused by rate $-q$ at $t = [t_1, t_2]$ reaches. Next, we will discuss the effect of the solutions of rate q at $t = [0, t_2]$ and rate $-q$ at $t = [t_1, t_2]$ on the pressure at distance r during falloff test ($t = [t_1, t_2]$).

Normally, it is easy to satisfy the condition that t_1 is far bigger than Δt. Therefore, we can assume three flow states during fall off test: a transient flow state when the pressure wave has not propagated to the outer boundary, a semi-steady state when the pressure wave has already propagated to the outer boundary and an intermediate state when the pressure wave has already propagated to the outer boundary but not reach semi-steady state. We will discuss the effect of q at $t = [0, t_2]$ and $-q$ at $t = [t_1, t_2]$ on the solution in each of the flow states.

(1) A transient flow state when the pressure wave has not propagated to the outer boundary:

For the transient flow state, based on equation (13), the solution caused by rate q at $t = [0, t_2]$ can be introduced as:

$$P_{r,t} = P_i + \frac{q\mu}{4\pi kh}\mathrm{ei}(X) \quad X = \frac{\phi\mu c_t r^2}{4k(t_1 + \Delta t)} \tag{16}$$

With the condition that t_1 is far bigger than Δt, we can obtain the approximation:

$$P_{r,t} \approx P_{r,t_1} \quad t_1 + \Delta t \approx t_1 \tag{17}$$

With the feasibility of approximation, we can imagine that the pressure changing rate $\mathrm{d}P_{r,t}/\mathrm{d}t$ is very small.

(2) A semi-steady state when the pressure wave has already propagated to the outer boundary:

For the semi-steady state, the pressure in reservoir can be predicted by the material balance equation as following:

$$c_t Ah\phi\left(\overline{P} - P_i\right) = qt \tag{18}$$

where A is the drainage area, h is the reservoir thickness, P_i is the initial reservoir pressure, $\overline{P}$ is the volume averaged pressure, q is the injection rate, t is the injection time. Equation (17) can be written as:

$$\frac{d\overline{P}}{dt} = \frac{q}{c_t Ah\phi} \tag{19}$$

From Equation (18), we can also assume that the pressure variation in reservoir will be very small as the drainage area is large enough.

(3) An intermediate state when the pressure wave has already propagated to the outer boundary but not reach semi-steady state:

Note, that if time t_1 is large enough, the flow state at the position not far from the wellbore can be represented as the semi-steady state even when the pressure wave has already propagated to the outer boundary but does not reach a semi-steady state yet.

Then, the change of pressure at distance *r* caused by rate *q* at $t = [0, t_2]$ will be slow. Note that, for the position *r*, which is far from wellbore and not propagated by the shut-in pressure wave yet, the pressure variation $\Delta P(r,t) = P(r,t) - P(r,t_1)$ still can be quite large if the interval Δt is big enough. The solution caused by rate $-q$ at $t = [t_1, t_2]$ can be approximated as:

$$P_{r,t} = P_i - \frac{q\mu}{4\pi kh}\mathrm{ei}(X) \quad X = \frac{\phi\mu c_t r^2}{4k\Delta t} \tag{20}$$

In contrast to the rate *q*, the rate $-q$ will cause the decrease of pressure at distance *r*. As referred above, the pressure changing rate $\mathrm{d}P_{r,t}/\mathrm{d}t$ caused by rate *q* will be relatively small and can be ignored. Therefore, it is reasonable to assume that the pressure at distance *r* will decrease as soon as the pressure wave caused by rate $-q$ at $t = [t_1, t_2]$ reaches this distance. Next, we will discuss how to apply the conclusions above for the interpretation of well test curve of CO_2 flooding.

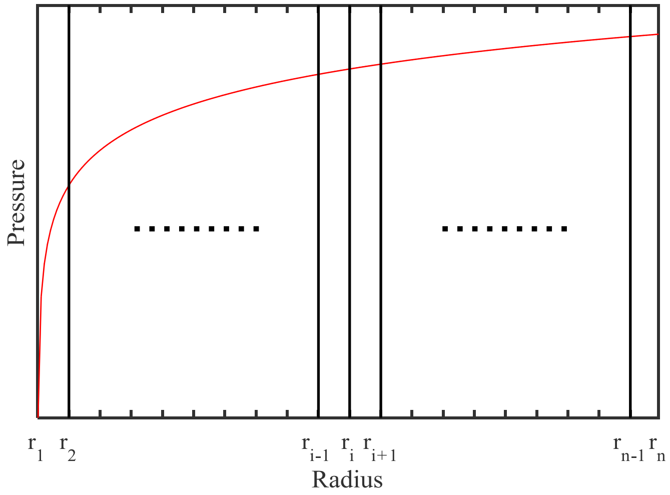

Fig. 26. The division of pressure profile.

It is well known that the characteristics of well test curve are mainly affected by the mean mobility of pressure wave propagated zone. As shown in Fig. 26, the reservoir is divided into (*n*-1) even segments in log space. To study the contribution of every segment to the mean mobility which will affect the characteristics of well test curve, we defined two variables as follows:

$$Q_{sum} = \sum_{i=1}^{i=n-1} q_i(r_{i+1} - r_i) = \sum_{i=1}^{i=n-1} \frac{2\pi k_i h(P_{i+1} - P_i)(r_{i+1} - r_i)}{\mu \ln(r_{i+1}/r_i)} \tag{21}$$

$$C_i = \frac{q_i(r_{i+1} - r_i)}{Q_{sum}} \tag{22}$$

where r_i represents the *i*th radius shown in Fig. 26; P_i represents the pressure at r_i; k_i represents the permeability of the segment between r_i and r_{i+1}; C_i can be represented as a contribution factor.

During steady state condition in a homogeneous reservoir, C_i will be equal to $1/(n-1)$ for every distance segment. But in a transient flow period, C_i will be different which will decrease when the segment is further from the wellbore. For the distance segment, to which the pressure wave just reached, the pressure difference $(P_{i+1} - P_i)$ will be small and lead to a small contribution factor. Therefore, the contribution of this segment to the mean mobility can be ignored. Based on equation (21), the contribution will be counted when the pressure difference becomes large enough. That can also be interpreted as the fact that the contribution factor for a given distance interval $[r_i; r_{i+1}]$ contributes only when the pressure begins to change observable.

In the conclusion to a fall-off test analysis: the space interval does not contribute to the mean mobility when the pressure wave just reaches the distance. Only starting at the time when the pressure begins to decrease observable, the interval mobility begins to contribute to the mean mobility and will be reflected in the well test curve.

Appendix B

The first challenge in discretization on a general unstructured 3D grid is how to obtain an accurate Well Index (WI) for the blocks perforated by well. To deal with this challenge, different meshing strategies around the wellbore for the 3D have been proposed in the past. The approach proposed by Karimi-Fard and Durlofsky (2012) is the most accurate for numerical solution but can result in a large number of small cells in the vicinity of well. The approach proposed by Artus et al. (2017) uses PEBI grid which becomes quite restrictive for a highly heterogeneous reservoir model. In our work, we present an accurate and flexible meshing strategy which follows the ideas suggested by Wolfsteiner and Durlofsky (2002).

First, we perform the unstructured gridding (Fig. 27) around the well keeping all important features and heterogeneity of the reservoir. In practice, the close vicinity of well can be characterized better than the rest of the reservoir using various short-range measurements such as different types of logs or micro-seismic. To preserve the resolution of near well data, we construct a region around the perforation interval and apply a single-phase upscaling inside it (Fig. 28a). For homogeneous reservoirs, this region has a cylindric form and a simple radial grid can be constructed analytically (Fig. 28b). For heterogeneous reservoir, iso-pressure aggregation (Karimi-Fard and Durlofsky, 2012) or solution based on Green-function (Artus et al., 2017) can be performed. To preserve the accuracy in well-test interpretation, the unstructured grid outside the region is kept unchanged. Next, we discretize and solve the governing equations base on the constructed hybrid 3D grid.

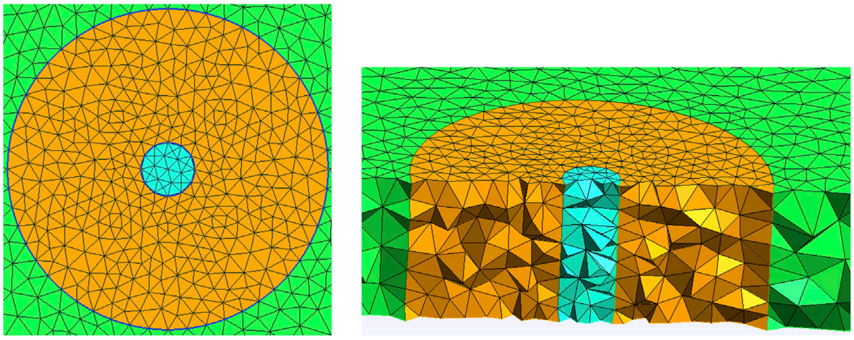

Fig. 27. The schematic of the mesh for 3D model.

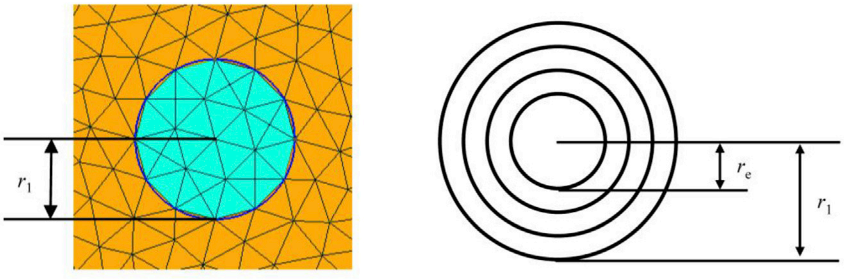

a) Original grids

b) New grids

Fig. 28. The objective region to perform aggregation.

To validate the accuracy of the new meshing strategy for a 3D unstructured grid, a simple radial model (Fig. 29) is implemented. The regions of radial grids near the wellbore shown in Fig. 28 are [0.1:0.1:1, 1:0.5:10]. We will compare the numerical and analytical solutions in the context of two-phase flow. First, obtain the water saturation profile shown in Fig. 30 based on the Buckley-Leverett theory with the parameters: $K_{rw} = S_w^2\,[1\text{-}(1\text{-}S_w)^2]$, $K_{ro} = S_o^4$, $\mu_o = 1.0$ cP, $\mu_w = 0.5$ cP, $q = 10$ m^3/d, $t = 30$ d, $h = 2$ m, $\phi = 0.2$, $r_w = 0.1$ m, $K = 0.01$ D. Second, with the saturation distribution, we can obtain the analytical pressure distribution based on the steady-state flow. Third, by mapping the saturation distribution in the 3D unstructured grid, we can obtain the numerical pressure distribution by discretizing and solving the two-phase flow governing equations at steady state. From the comparison between numerical and analytical solutions shown in Fig. 31, the proposed meshing strategy is considered as accurate enough to reproduce important features of two-phase flow.

To investigate the effect of grid size near the wellbore on the pressure distribution, a coarse grid has been constructed based on the grid shown in Fig. 29. The grid near the wellbore is changed as [2, 5, 10] and the grid in the rest region is kept unchanged. Fig. 31 shows that the grid resolution near the wellbore has a large effect on the pressure distribution. Therefore, one should be careful about the grid resolution near the wellbore during numerical simulation, especially for the well test simulation of multi-phase flow. Usually, we can refine the model around wellbore, but the refinement will lead to a large number of grid-blocks which will reduce the computational efficiency a lot. To deal with that, a flow based grid resolution analysis method is proposed which is focused on the well test of CO_2 flooding.

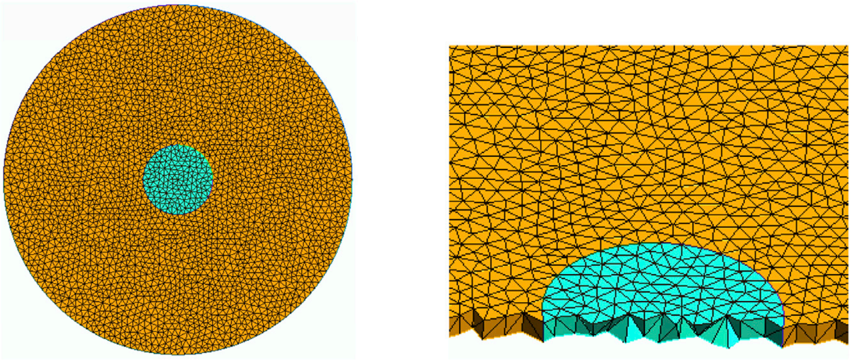

Fig. 29. The simple model to validate the accuracy of the new meshing strategy.

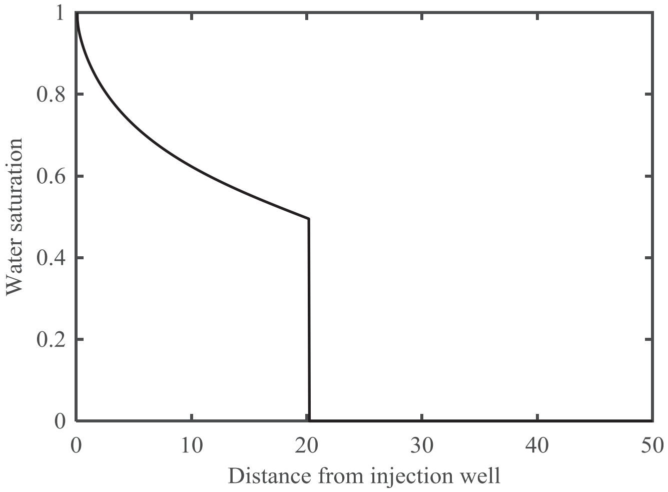

Fig. 30. The water saturation profile.

As the well test curve becomes sensitive in the CO_2 swept zone and even more sensitive in the two-phase region, we designed 4 injection strategies. Each of them corresponds to a specific position of the displacement front: 10–15 m, 15–25 m, 25–40 m and 40–60 m. Next, we perform a sensitivity analysis of well test curve to the meshing strategies for each position. The sensitivity analysis of 0–1 m and 1–10 m is included in the scenario when the displacement front is 10–15 m. Finally, we can combine all optimal strategies in one meshing scheme.

Based on the flow based grid resolution analysis method proposed above, we can determine a converge grid resolution for the well test simulation which is not only accurate enough but also computationally efficient. Fig. 32 shows the performance of the optimal grid resolution, very fine grid resolution and coarse grid resolution, of which the grid size is shown in Table 13. Compared with the coarse grid resolution, an accurate solution can be obtained with only 146% more grids in the near wellbore region (0–60 m) with the application of the flow based grid resolution analysis method, while the refined grid resolution needs 608% more grid-blocks. It is absolutely necessary to apply the optimal grid to reproduce the well test curve accurately and efficiently.

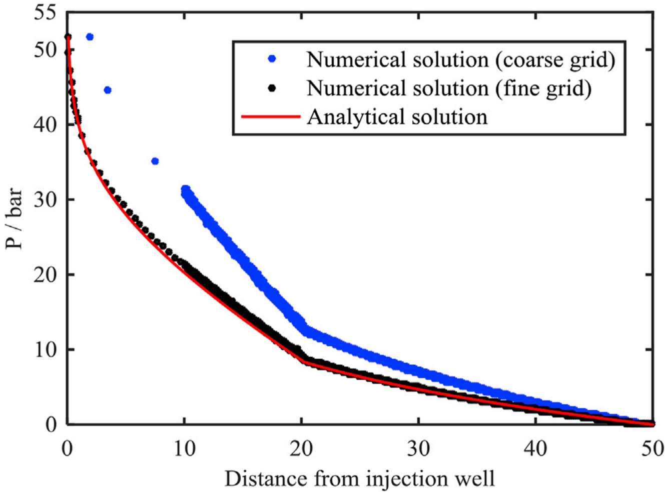

Fig. 31. The validation of the new meshing strategy.

Table 13
3 meshing strategies.

Region(m)	0–1	1–10	10–15	15–25	25–40	40–60	60–300
Optimal grid resolution	0.1:0.1:1	1:1:10	10:1.5:15	15:3:25	25:6:40	40:10:60	60:3:300
Refined grid resolution	0.1:0.05:1	1:0.5:10	10:0.5:15	15:1:25	25:1:40	40:1:60	60:3:300
Coarse grid resolution	0.1:0.3:1	1:3:10	10:5:15	15:5:25	25:8:40	40:20:60	60:3:300

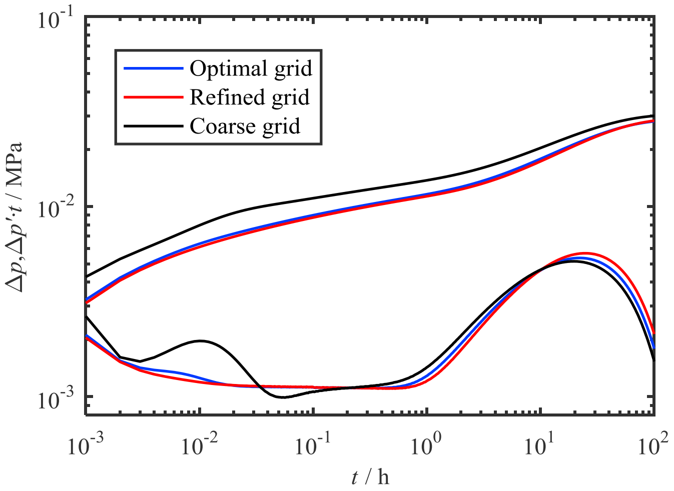

Fig. 32. The performance of the optimal, refined and coarse grid-blocks in region 0–60m.

References

Ambastha, A.K., 1989. Pressure Transient Analysis for Composite Systems. Stanford Univ., CA (USA).

Ambastha, A.K., 1995. Practical aspects of well test analysis under composite reservoir situations. J. Can. Petroleum Technol. 34 (05).

Araktingi, U.G., Orr Jr., F.M., 1990. Viscous fingering, gravity segregation, and reservoir heterogeneity in miscible displacements in vertical cross sections. In: SPE/DOE Enhanced Oil Recovery Symposium. Society of Petroleum Engineers.

Araman, A.W., Hoffman, M., Davis, T.L., 2008. Thief zone identification through seismic monitoring of a CO2 flood, Weyburn field, Saskatchewan. In: 2008 SEG Annual Meeting. Society of Exploration Geophysicists, Las Vegas, Nevada.

Artus, V., Fructus, D., Houzé, O., 2017. Simulation of Deviated Wells Using 3D Unstructured Grids of Flexible Resolution. SPE 182645-MS.

Bretz, R.E., Orr Jr., F.M., 1987. Interpretation of miscible displacements in laboratory cores. SPE Reserv. Eng. 2 (04), 492–500.

Brock, D.C., Orr Jr., F.M., 1991. Flow Visualization of Viscous Fingering in Heterogeneous Porous Media. SPE Annual Technical Conference and Exhibition. Society of Petroleum Engineers.

Cinar, Y., Jessen, K., Berenblyum, R., Juanes, R., Orr Jr., F.M., 2004. An experimental and numerical investigation of crossflow effects in two-phase displacements. In: SPE Annual Technical Conference and Exhibition. Society of Petroleum Engineers.

Claridge, E.L., Dietrich, J.K., 1983. Viscous Fingers and gravity tongues in CO2-steam stimulation. In: SPE California Regional Meeting. Society of Petroleum Engineers.

Davis, T., 2010. The state of EOR with CO2 and associated seismic monitoring. Lead. edge 29 (1), 31–33.

Eclipse Technical Description, Schlumberger, 2006.

Geuzaine, C., Remacle, J.-F., 2009. Gmsh: a three-dimensional finite element mesh generator with built-in pre- and post-processing facilities. Int. J. Numer. Methods Eng. 79 (11), 1309–1331.

Godec, M., Kuuskraa, V., Van Leeuwen, T., Melzer, L.S., Wildgust, N., 2011. CO2 storage in depleted oil fields: the worldwide potential for carbon dioxide enhanced oil recovery. Energy Procedia 4, 2162–2169.

Hemmati-Sarapardeh, A., Ayatollahi, S., Ghazanfari, M.H., Masihi, M., 2013. Experimental determination of interfacial tension and miscibility of the CO2–crude oil system; temperature, pressure, and composition effects. J. Chem. Eng. Data 59 (1), 61–69.

Holm, L.W., Josendal, V.A., 1982. Effect of oil composition on miscible-type displacement by carbon dioxide. Soc. Petroleum Eng. J. 22 (01), 87–98.

Iranshahr, A., Voskov, D.V., Tchelepi, H.A., 2013. Tie-simplex based compositional space parameterization: continuity and generalization to multiphase systems. AIChE J. 59 (5), 1684–1701.

Jessen, K., Orr Jr., F.M., 2004. Gas cycling and the development of miscibility in condensate reservoirs. SPE Reserv. Eval. Eng. 7 (5), 334–341.

Jiang, Y., 2008. Techniques for Modeling Complex Reservoirs and Advanced Wells (Doctoral dissertation). Stanford University.

Johns, R.T., Orr Jr., F.M., 1996. Miscible gas displacement of multicomponent oils. SPE J. 1 (1), 39–50.

Karimi-Fard, M., Durlofsky, L., 2012. Accurate resolution of near-well effects in upscaled models using flow-based unstructured local grid refinement. SPE J. 17 (04), 1084–1095.

Kazemi, H., Merrill, L.S., Jargon, J.R., 1972. Problems in Interpretation of Pressure Fall-off Tests in Reservoirs with and without Fluid Banks. SPE Journal 3696-PA.

Kendall, R.R., Winarsky, R., Davis, T.L., et al., 2003. 9C, 4D seismic processing for the Weyburn CO2 flood, Saskatchewan, Canada. In: SEG Annual Meeting. Society of Exploration Geophysicists, Dallas, Texas.

Kuuskraa, V.A., Koperna, G.J., 2006. Evaluating the Potential for 'game Changer' Improvements in Oil Recovery Efficiency from CO2 Enhanced Oil Recovery. Prepared for US Department of Energy, Office of Fossil Energy—Office of Oil and Natural Gas.

LaForce, T., Orr Jr., F.M., 2009. Four-component gas/water/oil displacements in one dimension: part III, development of miscibility. Transp. porous media 79 (2), 225–247.

Li, L., Yao, J., Li, Y., Wu, M., Zhang, L., 2016. Pressure-transient analysis of CO 2 flooding based on a compositional method. J. Nat. Gas Sci. Eng. 33, 30–36.

MacAllister, D.J., 1987. Pressure transient analysis of CO2 and enriched-gas injection and production wells. In: SPE Annual Technical Conference and Exhibition. Society of Petroleum Engineers Source, San Antonio, Texas.

Malik, Q.M., Islam, M.R., 2000. CO2 Injection in the Weyburn field of Canada: optimization of enhanced oil recovery and greenhouse gas storage with horizontal wells. In: SPE/DOE Improved Oil Recovery Symposium. Society of Petroleum Engineers.

Metcalfe, R.S., Yarborough, L., 1979. The effect of phase equilibria on the CO2 displacement mechanism. Soc. Petroleum Eng. J. 19 (04), 242–252.

Moortgat, J., 2016. Viscous and gravitational fingering in multiphase compositional and compressible flow. Adv. Water Resour. 89, 53–66.

NETL, N., 2010. Carbon Dioxide Enhanced Oil Recovery-untapped Domestic Energy Supply and Long Term Carbon Storage Solution. The Energy Lab.

Nordhaus, W.D., 1991. To slow or not to slow: the economics of the greenhouse effect. Econ. J. 101 (407), 920–937.

Orr Jr., F.M., Johns, R.T., Dindoruk, B., 1993. Development of miscibility in four-component CO2 floods. SPE Reserv. Eng. 8 (2), 135–142.

Orr Jr., F.M., Taber, J.J., 1984. Use of carbon dioxide in enhanced oil recovery. Science 224, 563–570.

Raef, A.E., Miller, R.D., Franseen, E.K., Byrnes, A.P., Watney, W.L., Harrison, W.E., 2005. 4D seismic to image a thin carbonate reservoir during a miscible CO2 flood: Hall-Gurney Field, Kansas, USA. Lead. Edge 24 (5), 521–526.

Satman, A., 1985. An Analytical Study of Interference in Composite Reservoirs. SPE Journal 10902-PA.

Schneider, S.H., 1989. The greenhouse effect: science and policy. Science 243 (4892), 771–781.

Su, K., Liao, X.W., Zhao, X.L., 2015. Transient pressure analysis and interpretation for analytical composite model of CO2 flooding. J. Petroleum Sci. Eng. 125, 128–135.

Sun, H., Yao, J., Gao, S., Fan, D., Wang, C., Sun, Z., 2013. Numerical study of CO2 enhanced natural gas recovery and sequestration in shale gas reservoirs. Int. J. Greenh. Gas Control 19, 406–419.

Tang, R.W., Ambastha, A.K., 1988. Analysis of CO2 pressure transient data with two-and three-region analytical radial composite models. In: SPE Annual Technical Conference and Exhibition. Society of Petroleum Engineers, Houston, Texas.

Tchelepi, H.A., Orr Jr., F.M., Rakotomalala, N., Salin, D., Woumeni, R., 1993. Dispersion, permeability heterogeneity, and viscous fingering: acoustic experimental observations and particle-tracking simulations. Phys. Fluids A Fluid Dyn. 5 (7), 1558–1574.

Terrell, M.J., Davis, T.L., Brown, L., et al., 2002. Seismic monitoring of a CO2 flood at Weyburn field, Saskatchewan, Canada: demonstrating the robustness of time-lapse seismology. In: 2002 SEG Annual Meeting. Society of Exploration Geophysicists, Salt Lake City, Utah.

Tian, S., Zhao, G., 2008. Monitoring and predicting CO2 flooding using material balance equations. J. Can. Petroleum Technol. 47 (11), 41–47.

Voskov, D., 2012. An extended natural variable formulation for compositional simulation based on tie-line parameterization. Transp. porous media 92 (3), 541–557.

Voskov, D.V., Tchelepi, H.A., 2012. Comparison of nonlinear formulations for two-phase multi-component EoS based simulation. J. Petrol. Sci. Eng 82-83, 101–111.

Walsh, J.W., Ramey, H.J., Brigham, W.E., 1981. Thermal Injection Well Falloff Testing. SPE 10227-MS.

Wolfsteiner, C., Durlofsky, L., 2002. Near-well Radial Upscaling for the Accurate Modeling of Nonconventional Wells. SPE-76779-MS..

Zhou, Y., Tchelepi, H.A., Mallison, B.T., 2011. Automatic differentiation framework for compositional simulation on unstructured grids with multi-point discretization schemes. In: SPE Reservoir Simulation Symposium, The Woodlands, Texas, USA.